Advances in Geo-Energy Research

Vol. 18, No. 2, p. 109-120, 2025

Original article

# Pore-scale simulation of permeability evolution induced by mineral precipitation during reactive transport

Heng Li[1,2,3], Fugang Wang[3]*, Tianhao Wu[1], Yilong Yuan[3], Huixing Zhu[3], Jie Liu[4]

[1]*Eastern Institute for Advanced Study, Eastern Institute of Technology, Ningbo, Zhejiang 315200, P. R. China*

[2]*Department of Modern Mechanics, University of Science and Technology of China, Hefei 230027, P. R. China*

[3]*Key Laboratory of Groundwater Resources and Environment, Ministry of Education, Jilin University, Changchun 130021, P. R. China*

[4]*Physical Science and Engineering Division, King Abdullah University of Science and Technology, Thuwal 23955-6900, Saudi Arabia*

**Keywords:**
Mineral precipitation
reactive transport
pore-scale simulation
crystal nucleation
porosity-permeability relationships

**Cited as:**
Li, H., Wang, F., Wu, T., Yuan, Y., Zhu, H., Liu, J. Pore-scale simulation of permeability evolution induced by mineral precipitation during reactive transport. Advances in Geo-Energy Research, 2025, 18(2): 109-120.
https://doi.org/10.46690/ager.2025.11.02

**Abstract:**
In order to examine the heterogeneous nucleation and growth dynamics of mineral precipitation in reactive transport systems, as well as the evolution of key upscaling parameters, such as porosity and permeability, this study employs a model that integrates pore-scale reactive transport with arbitrary Lagrangian-Eulerian method. This model incorporates a heterogeneous probabilistic nucleation process based on classical nucleation theory, which is used to parametrically simulate the nucleation and growth processes of individual mineral particles within the reactive transport. The findings indicate that fluid velocity, along with nucleation and mineral growth rates, plays critical roles in determining the pattern and spatial distribution of precipitates. Nucleation promotes irregularities in the precipitate pattern and reduces the influence of flow on the spatial distribution of precipitate formation across particle surfaces. Precipitation on the surface of a single mineral particle within a pore channel is more accurately governed by a power law model, which captures the evolutionary relationship between porosity and permeability in porous media with periodic structures.

## 1. Introduction

Reactive transport in porous media is integral to numerous natural and engineered processes, including geological $CO_2$ sequestration, sedimentary diagenesis, and oil and gas extraction (Loomer et al., 2021; Li et al., 2024a). For instance, during geological $CO_2$ sequestration, as $CO_2$-enriched acidic fluids traverse porous media, dissolution and precipitation reactions may occur at various stages. These processes may take place near the wellbore or within fractures of the caprock. In the first scenario, precipitation is unfavorable because it obstructs pore spaces, thereby decreasing the injection capacity of the reservoir, whereas dissolution enhances permeability and improves injection efficiency (Cohen et al., 2008). Conversely, in the latter scenario, precipitation proves beneficial as it prevents $CO_2$ leakage by sealing fractures within the caprock (Tian et al., 2019). In reactive transport studies, dissolution and precipitation reactions play a crucial role due to their impact on the hydrodynamic characteristics of porous media, particularly permeability. Variations in permeability directly influence fluid movement through porous media, thereby modifying solute transport and reaction rates. Pore-scale reactive transport modeling provides crucial insights into the coupled processes governing porous media. Although most current studies on pore-scale reactive transport primarily focus on mineral dissolution, research on mineral precipitation remains limited, especially concerning the evolution of porosity and permeability driven by precipitation (Li et al., 2025). Certain studies misrepresent the precipitation reaction as being merely

*Corresponding author.
*E-mail address*: hengli@eitech.edu.cn (H. Li); wangfugang@jlu.edu.cn (F. Wang); twu@eitech.edu.cn (T. Wu); yuanyl14@mails.jlu.edu.cn (Y. Yuan); zhuhx@jlu.edu.cn (H. Zhu); jie.liu.1@kaust.edu.sa (J. Liu).

Received August 16, 2025; revised September 11, 2025; accepted September 29, 2025; available online October 2, 2025.

Yandy Scientific Press

the inverse of dissolution, reflected in reaction rate equations solely by opposite signs, an approach that oversimplifies the complexity of the process (Steefel et al., 2013).

Existing studies have indicated that mineral precipitation reactions exemplify crystal nucleation and growth processes (Fazeli et al., 2020). In simulating mineral precipitation using reactive transport models, it is essential to incorporate nucleation, which is the initial stage of precipitation. In the process of nucleation, nuclei emerge from a supersaturated solution and subsequently experience growth, maturation, phase transformation, and crystallization. Nucleation can occur within the fluid phase, known as homogeneous nucleation, or at the fluid-solid interface, known as heterogeneous nucleation. However, few reactive transport models consider nucleation processes that start when a specified concentration threshold is reached. Despite these models being already quite advanced, they still have shortcomings when describing the nucleation process. By adopting the classical nucleation rate equation proposed based on the classical nucleation theory (CNT), the approximation of nucleation in the models can be further improved. According to the CNT, nucleation rates are contingent on factors such as supersaturation and interfacial free energy. Recent efforts have sought to integrate the CNT into reactive transport simulators, enabling simulations of wellbore integrity and cement chemistry alterations during $CO_2$ storage. Additionally, they aimed to explore how homogeneous and heterogeneous precipitation kinetics influence pore structure evolution in porous media (Li et al., 2017; Prasianakis et al., 2017).

Despite recent progress in incorporating nucleation processes into pore-scale reactive models, significant challenges remain, notably in accurately characterizing the dynamic evolution of the fluid-solid interface during precipitation, a critical factor in analyzing upscaled parameter evolution (e.g., porosity and permeability). Over the past decade, several numerical techniques have been developed to model mineral dissolution and precipitation processes with increasing accuracy. However, the nucleation process of the precipitation process has not been taken into account. Widely used methods are grounded in various numerical formulations, including the lattice-Boltzmann method, smooth particle hydrodynamics, and computational fluid dynamics based on finite difference, finite volume, or finite element techniques (Liu et al., 2022; Wang et al., 2023; Yang et al., 2024a). The leading interface-tracking techniques in multiphase computational fluid dynamics modeling include the volume-of-solid, level-set, phase-field, and arbitrary Lagrangian-Eulerian (ALE) methods (Li et al., 2023; Cai et al., 2024). The ALE method enables highly precise fluid-solid interface capture, as it requires no solid geometry assumptions; instead, the surface mesh dynamically adapts as the phase evolves, allowing the continuum mechanics governing equations to be solved with exceptional accuracy (Soulaine et al., 2017). However, the reliance of the ALE method on mesh reconfiguration limits its applicability to systems with few particles, as it cannot efficiently simulate pore-space evolution in large-particle systems and necessitates remeshing to preserve mesh quality after substantial shape deformations (Noiriel and Soulaine, 2021).

Furthermore, given that nucleation is inherently probabilistic, it may occur randomly throughout a region, even when physical conditions (e.g., supersaturation and temperature) remain constant (Fazeli et al., 2020; Starchenko, 2022; Yang et al., 2024b). Probabilistic nucleation results in varying spatial distributions of the precipitated phase, which in turn impacts system permeability. To achieve more reliable outcomes, an advanced reactive transport model ought to integrate the probabilistic characteristics of nucleation, like improved porosity-permeability relationships.

In this study, an inventive model that incorporates nucleation into a pore-scale reaction transport framework. The uniqueness of this method is in precisely capturing the probabilistic features of the CNT nucleation process. The proposed probabilistic nucleation model is implemented in dissolFOAM, an OpenFOAM®-based pore-scale reactive transport simulator that utilizes the ALE method for interface tracking (Starchenko, 2022). To enhance interface accuracy, an adaptive mesh refinement and staged mesh reconstruction technique is incorporated into the solver, enabling localized refinement and reconstruction near the flow-solid interface and partially addressing the ALE limitations. This simulator enables a parametric investigation of mineral nucleation and growth in reactive transport (e.g., altering growth rates and injection flow rates), allowing for the examination of related pore-permeability evolution rules, which were missing in previous pore - scale reactive transport models. Finally, the study summarizes the findings and outlines potential directions for future research.

## 2. Materials and Methods

### 2.1 Pore-scale reactive transport model

The incompressible Navier-Stokes equations describe the motion of fluid in the pore space:

$$\rho \nabla \cdot \boldsymbol{u} = 0 \tag{1}$$

$$\rho \left[ \frac{\partial \boldsymbol{u}}{\partial t} + (\boldsymbol{u} \cdot \nabla)\boldsymbol{u} \right] = -\nabla p + \mu \nabla^2 \boldsymbol{u} \tag{2}$$

where $\rho$ denotes the fluid density, $\boldsymbol{u}$ denotes the fluid velocity, $\nabla p$ denotes the pressure gradient, and $\mu$ is the dynamic viscosity.

The convection-diffusion equation describes the transport of reactants in the aqueous phase:

$$\frac{\partial c}{\partial t} + \nabla \cdot (\boldsymbol{u} c) = \nabla \cdot (D \nabla c) \tag{3}$$

where $c$ denotes the reactant concentration and $D$ is the molecular diffusion coefficient.

Non-homogeneous precipitation reactions are utilized as boundary conditions for the reaction surface. In this simplified model of mineral precipitation, a binary reaction is taken into account where the concentrations of anion A and cation B in a solution ascertain the saturation state of mineral AB within the solution, which can be denoted as:

$$A^- + B^+ \rightarrow AB \downarrow \tag{4}$$

Assuming species A and B possess equal concentrations and are thoroughly mixed at the inlet, and that the ions'

diffusion is with both ions having activity coefficients of 1. During mineral dissolution, the Onsager correction for diffusive transport has a marked impact, while during precipitation (Dutka et al., 2020; Yang et al., 2021), its effect is minor. However, it is not included in this work. Thus, Eq. (3) can be solved for only one kind of substance, and the saturated state $\Omega$ can be represented as:

$$\Omega = \frac{c^2}{c_{eq}^2} \tag{5}$$

where $c_{eq}$ represents the equilibrium ion concentration of a specific mineral.

The rate of surface reaction can be expressed in terms of local concentration as:

$$R = k_m(\Omega - 1) \tag{6}$$

In order to simulate the motion of mineral surfaces, the flow of mineral ions to the surface during precipitation needs to correspond with the reaction rate $R(c)$ (Szymczak and Ladd, 2012):

$$D\boldsymbol{n}\cdot\nabla c = R(c) \tag{7}$$

where $\boldsymbol{n}$ stands for the normal to the particle surface. In the precipitation process, the fluid-solid interface shifts. This is depicted by the boundary grid, which specifies the simulation domain and denotes the reaction surface. The nodes of the surface grid move with velocity $\boldsymbol{u}_\Gamma$:

$$v_m^{-1}\boldsymbol{u}_\Gamma = R(c)\boldsymbol{n} \tag{8}$$

where $v_m$ represents the molar volume of the mineral.

It should be noted that, in this study, to simplify the model, focus on the main contradiction (flow and reaction), and due to the limited computing resources, an isothermal model is selected, which assumes that the heat effect during the reaction process is very small and can be ignored, thus not considering the energy equation. This is a common and reasonable simplification. Therefore, the complexity of the model and the computational cost can be reduced, and the core mechanism of flow and reaction can be elucidated more clearly.

## 2.2 Probabilistic nucleation models

During mineral precipitation, nucleation can occur through classical or non-classical pathways. The non-classical ones include processes like prenucleation cluster formation, particle aggregation, and polycrystal transitions in minerals (De Yoreo et al., 2015), which are outside the scope of this study. The CNT suggests that for a stable nucleus to form, particles need to exceed a critical size to overcome the energy barrier resulting from the balance between the surface formation penalty and the total lattice volume energy of the particle. This research focuses on heterogeneous nucleation, where mineral formation happens on surfaces rather than in the solution. As per the CNT, the nucleation rate measures the number of particles that can nucleate over a certain surface area within a particular time period. The heterogeneous nucleation rate $J_s$ is reliant on the change in free energy (or nucleation energy barrier) $\Delta G$ during nucleation at the fluid-solid interface (Fernandez-Martinez et al., 2013; Li et al., 2014):

$$J_s = A\exp\left(-\frac{\Delta G}{k_B T}\right) \tag{9}$$

where $A$ represents the pre-exponential factor. It is a key kinetic parameter that can be understood as the number of collisions per unit volume and time between ions in the solution, as well as with the substrate, attempting to overcome the nucleation energy barrier $\Delta G$ (Fazeli et al., 2020; Yang et al., 2024b). In other words, it quantifies the "kinetic driving force" of nucleation events; a large $A$ value indicates that molecules have a high frequency of trying to form new phases, and even if the nucleation energy barrier is high, a considerable nucleation rate may still be observed. The value of $A$ in this model is based on literature data related to carbonate nucleation (Starchenko, 2022), which is in the order of $10^{-10} - 10^{-20}$. It should be noted that the $A$ factor is not constant but varies with temperature and the properties of the system itself (such as diffusion coefficients), which is also one of the main sources of uncertainty in CNT predictions. The parameter $k_B$ is the Boltzmann constant, and $\Delta G$ is a function of the interfacial free energy $\gamma$ and saturation $\Omega$:

$$\Delta G = \frac{\beta\left(v_m/N_A\right)^2\gamma^3}{\left(k_B T\ln\Omega\right)^2} \tag{10}$$

Here, $\beta = 16\pi/3$ represents the geometric factor and $N_A$ denotes the Avogadro number.

To incorporate nucleation into the model, it is presumed that individual nuclei cannot be broken down. Consequently, each face of the volumetric mesh, which defines the interface between the fluid and the solid, is marked as non-reactive until a nucleation event takes place. The probability of a random nucleation event occurring at time t can be represented by an exponential probability distribution function, namely, $J\exp(-Jt)$. The cumulative distribution function over time ($\Delta t$) is the integral of the probability distribution:

$$P = 1 - \exp(-J\Delta t) \tag{11}$$

Eq. (11) quantifies the probability of nucleation on a specific surface within the region $A_f$, where $J = A_f J_s$, $A_f$ represents the surface area of the nucleation substrate. Upon satisfying the nucleation condition, the surface is designated as reactive, and the boundary condition described by Eq. (7) is applied. The existing model fails to address the expansion of individual nuclei. Since a solitary nucleus can not fully envelop the surface, a surface coverage factor $\chi$ is brought in, signifying the proportion of each cell's coverage area to the entire surface area. Presuming that a lone nucleation occurrence produces a hemisphere with a surface area of 5 nm$^2$ and that nucleation adds much less to precipitation compared to mineral growth, the rise in the surface coverage factor is figured out from the growth rate in Eq. (8). Consequently, the shift in surface coverage for a particular cell at every time step can be articulated as:

$$\Delta\chi = \pi(\Delta r)^2 + \sqrt{\pi A_f \chi}\Delta r \tag{12}$$

where $\Delta r$ represents the increase in the radius of the hemi-

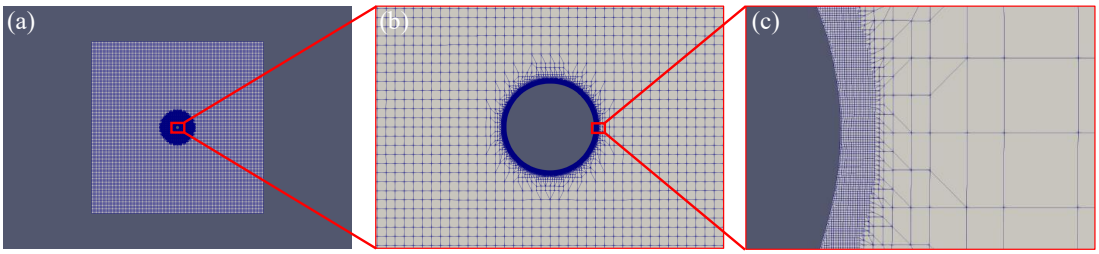


**Fig. 1**. Grid generation of the model. (a) Overall distribution of the model grid, (b) local densification of the grid near the particle and (c) re-densification of the grid on the particle surface.

sphere at a specific growth rate, which is expressed as:

$$\Delta r = \frac{v_m k t_d}{h_0} R \Delta t \tag{13}$$

The model offers a crude approximation of the real process and does not account for phenomena like multiple nucleation occurrences, anisotropy of crystal surface energy (which dictates the form of crystal particles), nucleus collisions, etc. Nevertheless, it enables a seamless shift from non-reactive to reactive surfaces when resolving individual nuclei is unattainable. The coverage of a specific surface fluctuates within the range $0 \leq \chi \leq 1$. The reaction speed on a partially covered surface is in proportion to the surface coverage ($R_{\text{part}} = \chi R$), resulting in inert surfaces at $\chi = 0$ and completely reactive surfaces at $\chi$=1. The nucleation speed is regulated by altering the pre-exponential factor $A$ in Eq. (9). The numerical implementation tools and relevant verifications of the model can be found in the Supporting Information.

## 2.3 Geometry and grid strategy for the model

The geometry employed in this study models spherical particles within a reaction flow (Fig. 1). In the reactive flow, particles have a radius of 10 μm, and the domain's total size is 1 mm. For simplifying visualization, speeding up computation, and capturing interface growth, two-dimensional simulations are performed. Notably, the current implementation is capable of simulating three-dimensional geometries without modifications, albeit with increased computational cost. The central particle is represented as a cylinder, confined between two parallel planes under empty boundary conditions. The boundaries perpendicular to the flow direction (top and bottom in Fig. 1(a)) are set with symmetric boundary conditions. The flow rate is imposed via a constant flow boundary condition. Boundary conditions were specified at the inlet (left side of Fig. 1(a)) with an inlet fluid velocity $u_{\text{in}}$ and at the outlet with zero static pressure. A no-slip boundary condition is imposed on the particle surface.

For the reactive transport equation (Eq. (2)), customized boundary conditions were applied on the reaction surface, adhering to the mass balance (Eq. (7)) and reaction rate (Eq. (6)). Additionally, when nucleation is enabled, the rate is scaled proportional to the nucleation parameter $\chi$. The concentration field is normalized with respect to the reactant concentration cin at the inlet, such that a Dirichlet boundary condition of 1 is imposed at the inlet. Further details regarding the implementation of the custom Robin boundary condition on the particle reaction surface are provided by Starchenko et al. (2016). A Neumann boundary condition with a zero gradient is enforced at the outlet. At the reactive interface, the boundary condition for the concentration field is implemented as a codedMixed boundary condition. The current implementation is exactly the same as that for the dissolFoam solver, except for the reaction rate expression. The implementation is well described in Starchenko et al. (2016). Here, the details regarding nucleation are clarified.

To speed up the calculation, non-uniform grids are used in this study. Fig. 1(b) shows an enlarged area near the particles to show mesh refinement near the surface. The purpose of mesh refinement is to capture features resulting from the unsteady growth of the interface, and Fig. 1(c) further shows the enlarged area around the particle surface. All meshes were generated using the meshing tool snappyHexMesh. In simple terms, the two-dimensional simulation domain is divided into $320 \times 320$ cells, and then six times the mesh refinement is performed around the particle surface. Due to the irregular growth of the surface during the precipitation process, the grid becomes highly distorted and needs remeshing, so the total number of grids is not fixed during the simulation process and it will continue to increase. Considering the calculation time, the total number of grids in the simulation process is limited to less than 300,000.

It should be noted that the refinement of a six-level grid is a necessary condition for accurate simulation but not a sufficient one. It mainly solves the problem of geometric resolution, while to accurately reflect reaction rates, it is also necessary to address the issues of boundary layer resolution and chemical reaction models. The dynamic remeshing process itself is designed to ensure that, as the shape of particles changes, there is always a sufficiently fine grid surrounding them, which is the basis for obtaining credible results. Therefore, dynamic remeshing provides a necessary and dynamically adaptive geometric framework that makes the accurate calculation of reaction rates possible. However, whether it can ultimately accurately reflect depends on whether the boundary layer is sufficiently resolved and whether the chemical reaction model used itself is accurate. Besides, precipitation is a complex process involving nucleation and crystal growth/dissolution, which may change the morphology and size of particles. Dynamic remeshing has the advantage of being able to adapt to such geometric changes. Furthermore, the rate of crystal growth strongly depends on the supersaturation at the interfa-

**Table 1**. Parameters used in the simulation.

| Parameter | Symbol | Value |
|---|---|---|
| Diffusion coefficient | $D$ | $1.4 \times 10^{-5}$ cm$^2$/s |
| Molar mass | $M$ | 100.09 g/mol |
| Molar volume | $v_m$ | 37 cm$^3$/mol |
| Inlet concentration | $c_{in}$ | $6.6 \times 10^{-3}$ mol/L |
| Equilibrium concentration | $c_{eq}$ | $0.58 \times 10^{-4}$ mol/L |
| Interfacial free energy | $\gamma$ | 35 mJ/m$^2$ |
| Unit length | $h_0$ | $1.0 \times 10^{-3}$ cm |
| Dynamic viscosity | $\mu$ | $1.0 \times 10^{-3}$ Pa·s |
| Temperature | $T$ | 298.15 K |
| Solvent density | $\rho$ | 0.997 g/cm$^3$ |

ce. Only with sufficiently fine grids can the true supersaturation at the interface be accurately calculated, rather than an average diluted by the surrounding fluid. Moreover, even if the grid is very fine, if the precipitation kinetics model (such as what function the growth rate is of supersaturation) itself is inaccurate, or if it involves anisotropic growth, there will still be deviations in the calculation results.

## 3. Results and discussion

Calcite ($CaCO_3$) was selected as the reference material for precipitation. The process of calcite precipitation is complex, being affected by various factors such as $CO_2$ pressure and solution pH, etc. Moreover, the precipitation of $CaCO_3$ can lead to the formation of different polycrystalline structures, including amorphous calcium carbonate. To make the pore-scale reactive transport model suitable for multiphase reactions and dynamic interface coupling, the simplest surface reaction model was used. The equilibrium concentration of calcite is approximately the square root of the equilibrium constant (Plummer and Busenberg, 1982). These assumptions and simplifications cause the system to not completely capture the real conditions of calcite mineral precipitation. The parameters used in this work need to be reasonable and representative enough of a realistic system. Nevertheless, modeling the precipitation of specific minerals requires the careful inspection of parameters like the reaction rate constant, and modifications such as using ion activity rather than concentration may be essential for accurately calculating the solute diffusion capacity and local saturation states.

Usually, a series of dimensionless numbers are set to examine dynamic processes governed by flow states and reaction speeds. This research centers on the contest between reaction and transport at relatively low flow velocities. Consequently, the most significant dimensionless numbers are the Pèclet (Pe) number and the Damköhler (Da) number, which stand for the proportion of flow velocity to diffusion velocity and reaction velocity to diffusion velocity, respectively, as shown below:

$$\mathrm{Pe} = \frac{u_{\mathrm{in}} h_0}{D} \tag{14}$$

$$\mathrm{Da} = \frac{h_0 v_m R(c_{\mathrm{in}})}{D} \tag{15}$$

where $u_{\mathrm{in}}$ denotes the inflow rate and $R(c_{\mathrm{in}})$ stands for the reaction rate (related to the inflow concentration). For efficiently altering the Da and Pe values, it is necessary to modify the reaction rate constant $k_m$ and the inflow rate. Though the reaction rate constant of calcite precipitation is $k_{m,\mathrm{calcite}} = 3.81 \times 10^{-11}$ mol/cm$^2$/s (Nilsson and Sternbeck, 1999), in parametric investigations, $k_m$ ranges from $10^{-4}$ to $10^{-10}$ mol/cm$^2$/s, and $u_{\mathrm{in}}$ changes between 0.01 and 10 cm/s. The values of other pertinent simulation parameters are presented in Table 1.

### 3.1 Precipitation growth

Initially, the precipitation process is simulated without accounting for nucleation, meaning that precipitation occurs on all particle surfaces (the radius of the particles is 10 μm), a common approach in previous studies of this nature. Fig. 2 presents the precipitation results under varying flow rates and reaction rates. The simulated images were captured at different time points and uniformly scaled for comparative analysis. Mullins and Sekerka (1964) demonstrated that rapidly growing interfaces produce wavelength perturbations unconstrained by a lower limit, a phenomenon known as Mullins-Sekerka instability. In parametric investigations, both the flow rate and the reaction rate dictate the condition of mineral precipitation. The rates manage the initiation of instability as the reaction interface evolves. Fig. 2 shows that with an increase in Da and Pe numbers, the count of growth features goes up and the level of instability becomes more intense. These outcomes align with prior discoveries regarding Mullins-Sekerka instability, suggesting that quicker surface growth results in more instability (Langer, 1980). These instances illustrate that this impact can be attained either by boosting the reaction rate constant, thus strengthening the reaction, or by augmenting the transport of reactants to the solid surface, like through a heightened flow rate.

Moreover, as the Pe number increases, the diffusion layer surrounding the reactive particles becomes thinner, thereby enhancing reactant transport to the particle interface. Consequently, the wavelength of instabilities decreases, corresponding to elevated reaction rates. Across all Da numbers, increased fluid velocity amplifies the anisotropy of sediment formation. On the fluid-exposed surface of the particles, sediment growth is more rapid on the frontal side. The quantity of reactant reaching the rear of the particle diminishes due to consumption during precipitation on the frontal surface; consequently, the reaction rate on the rear side is reduced. As illustrated in Fig. 2 (Pe = 7.14 and Da = 3,440, Pe = 7.14 and Da = 34.4), a primary dense precipitated layer forms around the initial particles, branching towards dendrites. However, the thickness of this primary layer is influenced by both reaction and flow rates. At low Da and Pe numbers, the primary layer thickens, potentially influenced by surface roughness or defects in real systems. Once dendrites have started to grow, the primary layer's expansion slows and eventually ceases. As dendrites continue to grow, they deplete the available reactants, thereby shielding the primary layer and giving rise to a porous secondary precipitate.

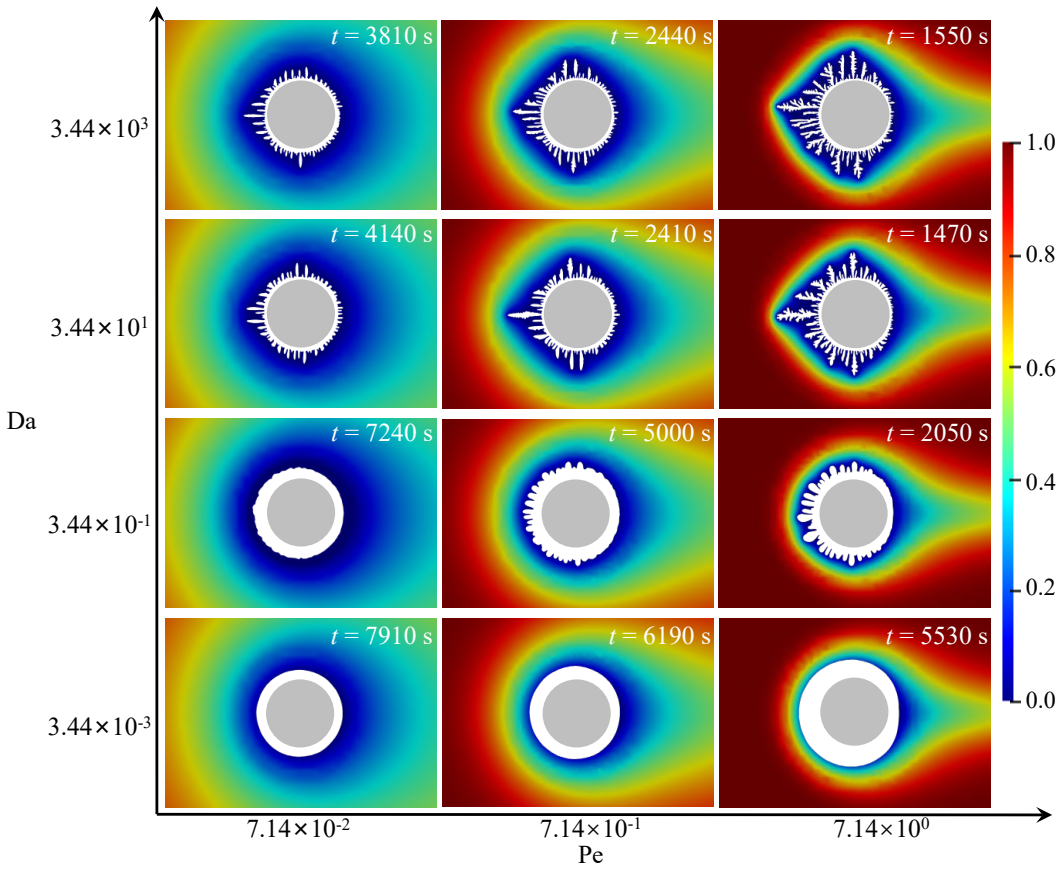


**Fig. 2**. Particle surface precipitation patterns and the distribution of reactant concentrations without considering nucleation. Gray indicates initial particles and white indicates precipitation.

## 3.2 Precipitation nucleation growth

To investigate the coupling between surface growth and nucleation, the development of surface deposits in particle flow was analyzed by comparing scenarios with nucleation "on" and "off" under different reaction rates (Fig. 3). When the nucleation switch is "on", the solver modifies the boundary conditions for particles within the flow, making the initial surface inert (i.e., having a reaction rate of zero), and after nucleation, nucleation becomes proportional to the surface coverage as described in Section 2.2. In simpler geometries, such as channel flow, estimating the effective reaction rate while accounting for diffusion resistance is feasible. However, for more complex geometries, such as mineral particles in flow, such corrections remain approximate. While diffusion hindrance within the interface layers was not analyzed in depth in this study, it presents an intriguing avenue for future research, particularly regarding charged surfaces.

As nucleation on the initial surface is inert, the concentration surrounding the particle initially mirrors that at the inlet. Once nucleation occurs, the surface grid becomes reactive, with the nucleation site locally depleting reactants. Nucleation influences precipitation distribution at both low and high reaction rates, ultimately accelerating surface growth instability. As the reaction rate increases, so does the significance, as depicted in Fig. 3. Interestingly, while nucleation accelerates growth at specific sites, leading to irregular sediment shapes, growth in the absence of nucleation yields more porous sediments characterized by smaller dendrites, as seen in Fig. 3 (Pe = 71.4 and Da = 34.4, Pe = 7.14 and Da = 34.4). This indicates that nucleation not only reduces porosity but also fosters uneven sediment formation and distribution.

As illustrated in Fig. 2, higher flow rates effectively enhance surface reaction rates while reducing dendrite width. Fig. 3 further demonstrates the impact of nucleation rate on sediment morphology across various flow rates. Comparing the low flow velocity at Pe = 0.714 with the high flow velocity at Pe = 71.4 reveals that, across all nucleation rate values, growth feature width decreases slightly with reduced flow velocity. Notably, as the nucleation rate diminishes, the asymmetry in the precipitated phase induced by flow direction also becomes reduced. Fig. 3 illustrates that, at $\ln A = 15$, flow direction exerts minimal influence on the quantity of precipitate formed on the front or back of the particles. However, at lower nucleation rates ($\ln A = 20$) or when nucleation is absent, the effect turns more distinct, similar to the "off" nucleation situation.

## 3.3 Upscaling relationship between porosity and permeability

Establishing an accurate constitutive relationship between permeability and porosity is essential for macroscopic continuum-scale simulations. Such simulations of reactive

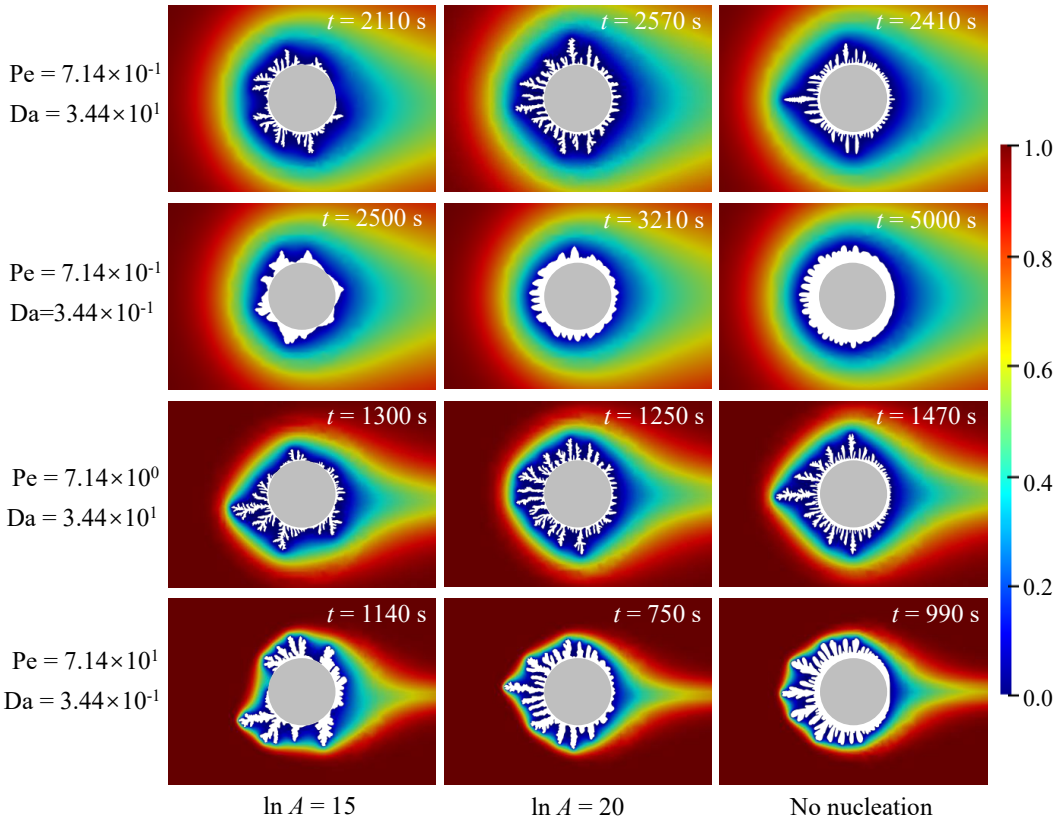


**Fig. 3**. Particle surface precipitation patterns and distribution of reactant concentrations, where the left two columns of nucleation are "on", and the right column of nucleation is "off".

transport in porous media rely on several spatially averaged transport equations. Upscaled parameters, such as permeability and porosity, are employed in these equations to encapsulate the averaged effects of intricate pore-scale processes. In this study, it is assumed that a single circular particle governs the permeability and porosity variations within a $50 \times 50$ μm representative elementary volume, with the particle centered within the representative elementary volume. It should be noted that the calculation domain of $50 \times 50$ μm is not strictly limited. This size of pore permeability calculation domain is chosen mainly to be able to describe the changes on the particle surface and the process of pore permeability evolution at an appropriate microscopic scale. Furthermore, this size satisfies the theoretical assumption of periodic homogenization of porous media to the least possible extent (Ray et al., 2012; Gärttner et al., 2020). The theoretical basis of the periodic homogenization method is the assumption that the microstructure of porous media is periodic, that is, the repetition of a basic unit whose size and complexity depend on the actual microstructure (Bourbatache et al., 2012). Generally speaking, even if this assumption has never been precisely verified, if the basic unit is complex enough and constitutes a REV, it achieves a good approximation of real porous media (Bourbatache et al., 2023). The pore volume (porosity) can be derived from the volumes of both the particle and the sediment, while permeability is determined using Darcy's law. According to Darcy's law, permeability is a constant coefficient that characterizes the relationship between fluid properties, flow and the parameters of the porous material, and it is computed as follows (Li et al., 2024b):

$$k = \frac{Q\mu L}{S\Delta P} \tag{16}$$

where $k$ stands for the permeability, $\Delta P$ represents the pressure difference applied across the medium, $L$ denotes the medium's length in the flow direction, and $Q$ is the outlet flow rate.

For porous media, permeability can usually be estimated using the Kozeny-Carman (KC) law or the power law, which are expressed as (Li et al., 2010; Tian and Wang, 2018):

$$k_{KC} = \frac{n^3}{(1-n)^2 M^2 d} \tag{17}$$

$$k_P = n^m \tag{18}$$

where $k_{KC}$ and $k_P$ stand for the forecasted permeability, $n$ stands for the porosity, $M$ stands for the specific surface area (the ratio of area to volume) of the medium, $d$ stands for the Kozeny constant (which is associated with the geometry of the channel in the porous medium), and $m$ represents the fitting factor. By normalizing Eqs. (16)-(18), the following equations can be obtained:

$$\frac{k}{k_0} = \frac{Q\Delta P}{Q_0 \Delta P_0} \tag{19}$$

$$\frac{k_{KC}}{k_{0KC}} = \left(\frac{n}{n_0}\right)^3 \left[\frac{(1-n_0)M_0}{(1-n)M}\right]^2 \tag{20}$$

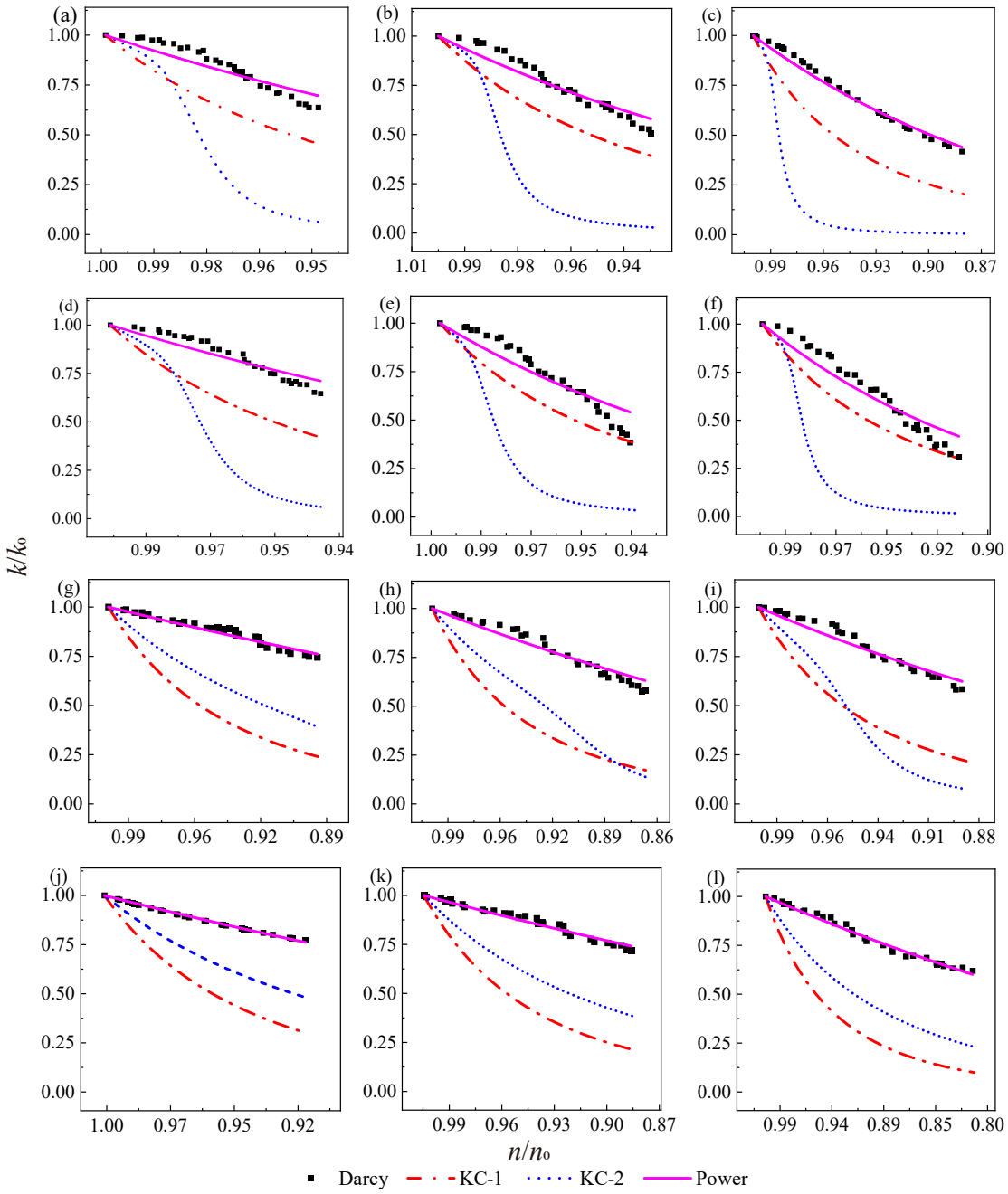


**Fig. 4**. Relationship between normalized porosity and normalized permeability. (a) Pe =0.0714 and Da=3440, (b) Pe =0.714 and Da=3440, (c) Pe =7.14 and Da=3440, (d) Pe =0.0714 and Da=34.4, (e) Pe =0.714 and Da=34.4, (f) Pe =7.14 and Da=34.4, (g) Pe =0.0714 and Da=0.344, (h) Pe =0.714 and Da=0.344, (i) Pe =7.14 and Da=0.344, (j) Pe =0.0714 and Da=0.00344, (k) Pe =0.714 and Da=0.00344, (l) Pe =7.14 and Da=0.00344.

$$\frac{k_P}{k_{0P}} = \left(\frac{n}{n_0}\right)^m \tag{21}$$

where $k_0$ represents the initial permeability, $\Delta P_0$ stands for the initial pressure difference, $k_{0KC}$ is the initial predicted permeability, $n_0$ indicates the initial porosity, and $M_0$ denotes the initial specific surface area of the medium. Eqs. (19)-(21) are utilized to compute the relative change between the measured and predicted permeability. Since Eq. (19) accounts for the variation in specific surface area while calculating the empirical relative permeability, the surface sediment morphology varies across all parameterized study cases. Therefore, when utilizing the KC law to predict permeability, the outcomes vary in each instance. To put it another way, if the change in specific surface area is not taken into account in Eq. (19), the predicted permeability, computed through the KC law, stays the same in all cases, as illustrated in Figs. 4 and 5.

For the simulation cases without considering the factor of nucleation, the normalized evolution of porosity and permeability is shown in Fig. 4, where the scattered dots represents the results from Eq. (19), the dotted-dashed line shows the

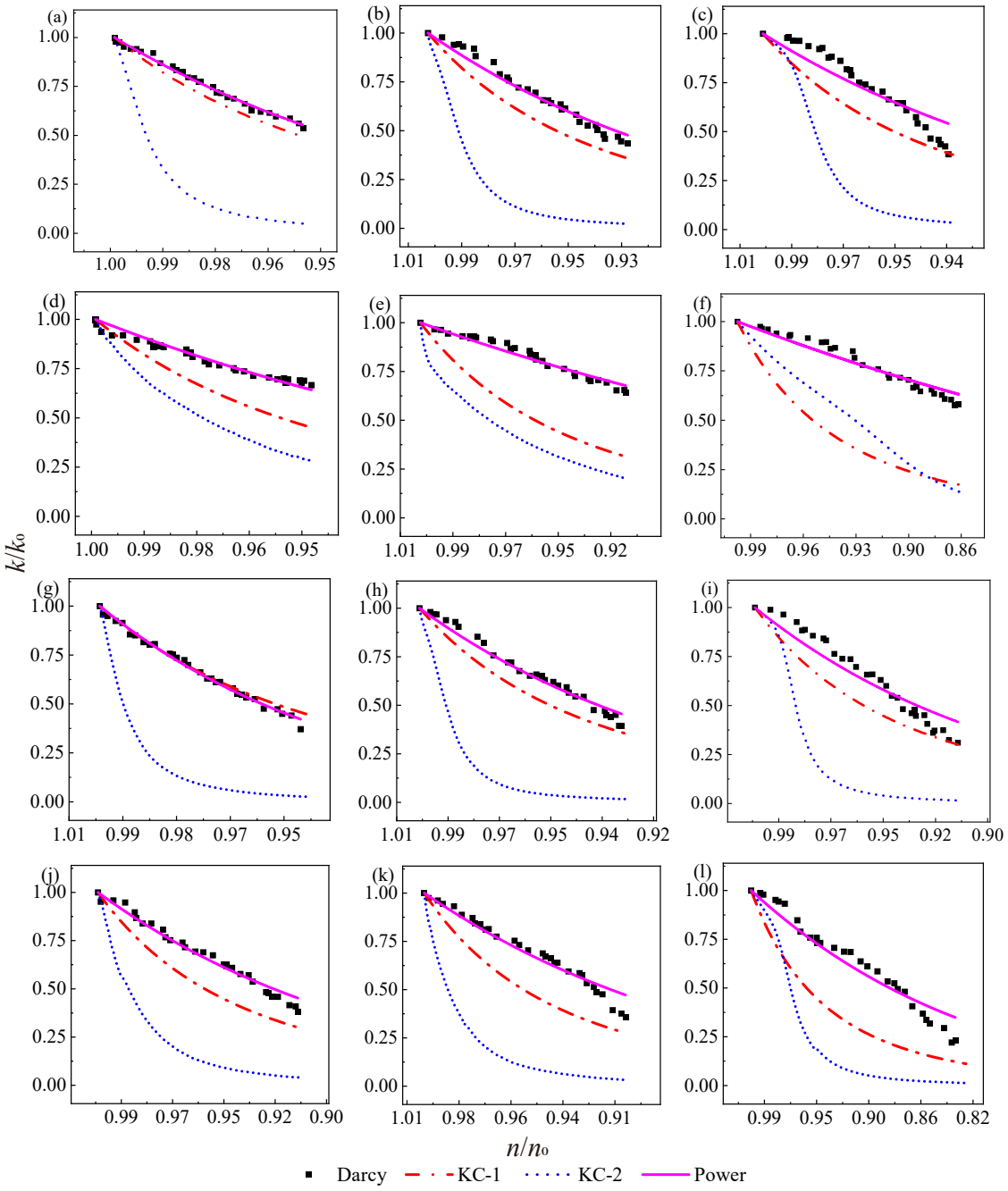


**Fig. 5**. Relationship between normalized porosity and normalized permeability under nucleation "on" and "off" conditions. (a), (b) and (c) Pe =0.714 and Da=34.4; (d), (e) and (f) Pe =0.714 and Da=0.344; (g), (h) and (i) Pe =7.14 and Da=34.4; (j), (k) and (l) Pe =71.4 and Da=0.344.

results from Eq. (20) without accounting for specific surface area, the dotted line displays the results from Eq. (20), and the solid line illustrates the results from Eq. (21). The Pe and Da numbers for each subgraph in Fig. 4 correspond to the respective subgraph in Fig. 2. The power law proves to be more accurate in predicting permeability, whereas the prediction outcomes of the two KC laws are suboptimal. As shown in Fig. 4, the KC law, that accounts for changes in specific surface area, exhibits a trend where the predicted permeability decline first decelerates, then accelerates, and finally slows down once the permeability approaches zero. This relatively complex behavior is primarily driven by the changes in specific surface area. Fig. 2 demonstrate that the number of dendrites is substantially greater than that in other simulated cases, and naturally, the greater the number of dendrites is, the larger the specific surface area. Consequently, during the precipitation growth process, $M_0/M$ gradually decreases and approaches zero. When specific surface area changes are considered, the KC law is not well-suited to describe the evolution of porosity and permeability during mineral precipitation. While the KC

**Table 2**. Results of regression analysis without nucleation scenario.

| Parameter | Pe = 0.0714 | | Pe = 0.714 | | Pe = 7.14 | |
|---|---|---|---|---|---|---|
| | *m* | $R^2$ | *m* | $R^2$ | *m* | $R^2$ |
| Da = 344 | 6.71 | 0.867 | 8.23 | 0.923 | 6.49 | 0.984 |
| Da = 34.4 | 5.63 | 0.886 | 9.19 | 0.877 | 9.81 | 0.918 |
| Da = 0.344 | 2.46 | 0.956 | 3.18 | 0.943 | 4.02 | 0.941 |
| Da = 0.00344 | 3.06 | 0.996 | 2.46 | 0.969 | 2.45 | 0.986 |

**Table 3**. Results of regression analysis considering nucleation and without nucleation.

| Parameter | $\ln A = 15$ | | $\ln A = 20$ | | No nucleation | |
|---|---|---|---|---|---|---|
| | *m* | $R^2$ | *m* | $R^2$ | *m* | $R^2$ |
| Pe = 0.714<br>Da = 34.4 | 12.42 | 0.994 | 10.02 | 0.967 | 9.19 | 0.877 |
| Pe = 0.714<br>Da = 0.344 | 8.07 | 0.945 | 4.55 | 0.956 | 3.18 | 0.943 |
| Pe = 7.14<br>Da = 34.4 | 16.05 | 0.993 | 10.70 | 0.978 | 9.81 | 0.918 |
| Pe = 71.4<br>Da = 0.344 | 8.86 | 0.980 | 7.70 | 0.954 | 5.71 | 0.943 |

law without specific surface area considerations yields better results than the version that accounts for it, its predictions are still far from the measured values. Furthermore, the predicted results are consistent across all cases, failing to capture the influence of varying pore structures on permeability, making it an inadequate representation of reality.

The Pe and Da numbers for each subgraph in Fig. 5 corresponds directly to the subgraphs in Fig. 3. It is evident that the power law remains the more accurate approach in predicting permeability within the nucleation scenario when compared to both KC laws. As depicted in Figs. 5(a) and 5(g), under a specific Da number, Pe number, and nucleation conditions, the KC law without accounting for changes in the specific surface area exhibits reasonable accuracy in predicting permeability, which is particularly obvious in Fig. 5(g). Obviously, the permeability predictions align well with the power law. Furthermore, under the nucleation scenario, the KC law that incorporates changes in the specific surface area shows a trend of rapid initial decline followed by a slower descent in permeability prediction. Compared to the corresponding simulation without nucleation, the initial slow descent is absent, primarily because the nucleation process leads to reduced porosity (as shown in Fig. 3), which accelerates the increase in specific surface area. It is worth noting that permeability does not continuously decrease as the porosity reduces. As shown in Fig. 4(b), there is a local increase near $n/n_0 = 0.95$. This phenomenon occurs mainly because the entire simulation process is not continuous but consists of many simulation periodicities. In the process of numerical implementation, remeshing and the interpolation of volume domain mapping between the new and old grids cause slight deviations in the velocity and pressure used to calculate the permeability between adjacent simulation periods, resulting in a brief and slight increase in permeability. However, from an overall perspective, this does not affect the trend that permeability decreases with the reduction of porosity.

In Figs. 4 and 5, the measured permeability shows fluctuations of varying degrees, which are essentially dynamic manifestations of microstructural changes in macroscopic parameters. These are closely related to factors such as particle morphology, growth pattern of the precipitation layer, and flow heterogeneity, among which there are mainly two specific reasons. Firstly, the irregular variation in particle shape is the main cause of permeability fluctuation, and this fluctuation is positively correlated with the irregularity of the fluid-solid interface. Therefore, the smoother the interface is, the smaller the permeability fluctuation. Secondly, the deviations resulting from remeshing and mapping interpolation in each simulation periodicity can also cause fluctuations in permeability. In contrast, it can be seen that the permeability fluctuation in Fig. 4(j) is the smallest and is relatively smooth. This is because the corresponding Fig. 2 (Pe = 0.0714 and Da = 0.00344) has the slowest and most stable interface movement speed among all the simulation cases.

When considering both Figs. 4 and 5, it becomes evident that, in comparison to the KC law, the power law provides a more accurate description of the porosity-permeability relationship during mineral precipitation. However, determining the fitting factor *m* in the power law remains a significant challenge. To quantitatively assess the accuracy of the power law in describing the porosity-permeability relationship and to investigate the variability of the fitting factor *m*, regression analysis is conducted between the predicted and observed values of the power law. The coefficient of determination, denoted as $R^2$, is used to assess the goodness of fit between the two variables. Detailed fitting results, including the value of $R^2$, can be found in the Tables 2 and 3. The results indicate that the value of the fitting factor *m* is associated with the heterogeneity of precipitation formation and distribution. The more intricate the structural characteristics of the precipitate is, the larger the *m* value tends to be. In simpler terms, the specific surface area is directly proportional to the value of *m*, that is, $m \propto M$.

In this work, the KC law and the power law are selected for comparison. The KC law, as a classic porosity-permeability model, is widely utilized and often serves as a benchmark reference. Although the KC law does not have fitting parameters, it also includes those related to the properties of the medium, such as porosity and specific surface area. In contrast, the fitting parameters in the power law model are designed to quantify the nonlinear relationships observed in the experiments, and their numerical ranges are subject to physical constraints. Despite the quantity and type of parameters of the two models being different, they are applied based on their respective theoretical frameworks, and they are all related to the physical mechanism. It should be noted that, in fact, most porosity-permeability laws are only justified

where detailed process knowledge is available (Hommel et al., 2018). Therefore, it is considered that any knowledge about the details of the processes leading to the modification of the porous medium can justify the development of a specific porosity-permeability relation for the particular process under the conditions of interest.

## 4. Conclusions

This paper presents a model that integrates pore-scale reactive transport with the ALE method to simulate interfacial dynamics during mineral precipitation. This model incorporates a heterogeneous probabilistic nucleation process based on the CNT and enables the precise quantification of porosity-permeability evolution under varied flow, reaction, and nucleation conditions. Initial simulations, excluding nucleation, focus on the effects of reaction and flow rates on precipitation morphology. The results show that high Da and Pe numbers lead to Mullins-Sekerka instabilities and the thinning of dense precipitate layer, while secondary porous precipitates grow more rapidly due to instability, resulting in complex structures.

When nucleation is considered, surface growth instability is enhanced, promoting irregularly shaped precipitates. Low nucleation rates reduce the asymmetry of precipitation across the particle surface, while high nucleation rates or no nucleation result in more uniform growth. The study also analyzes porosity and permeability evolution, concluding that the widely used KC law is insufficient for predicting permeability changes during precipitation, particularly due to variations in the specific surface area. In contrast, a power law model more accurately captures the porosity-permeability relationship, with the fitting factor correlating positively with specific surface area. Further investigation into the mathematical relationship between the fitting factor and specific surface area is recommended for more complex pore geometries.

Although this study primarily focuses on mineral growth and nucleation in the reaction flow of single-particle systems, the methods developed and the conclusions obtained have significant implications for understanding more complex multi-particle systems. Specifically, the exploration at the single-particle scale can provide information and expansion paths for research on multi-particle systems from the following aspects: i) As a benchmark and validation basis; ii) revealing core physical mechanisms; iii) providing simplification strategies for multi-particle modeling; iv) guiding the development of multi-scale computational methods; v) parametric studies and upscaling laws.

## Acknowledgements

This work was supported by the National Natural Science Foundation of China (Nos. 42502252, U2244215 and 42472320) and the Key Laboratory of Groundwater Resources and Environment (Jilin University), Ministry of Education.

## Supplementary file

https://doi.org/10.46690/ager.2025.11.02

## Conflict of interest

The authors declare no competing interest.



## References

Bourbatache, K., Millet, O., Aït-Mokhtar, A., et al. Modeling the chlorides transport in cementitious materials by periodic homogenization. Transport in Porous Media, 2012, 94(1): 437-459.

Bourbatache, K., Millet, O., Moyne, C. Upscaling coupled heterogeneous diffusion reaction equations in porous media. Acta Mechanica, 2023, 234(6): 2293-2314.

Cai, J., Jiao, X., Wang, H., et al. Multiphase fluid-rock interactions and flow behaviors in shale nanopores: A comprehensive review. Earth-Science Reviews, 2024, 257: 104884.

Cohen, C. E., Ding, D., Quintard, M., et al. From pore scale to wellbore scale: Impact of geometry on wormhole growth in carbonate acidization. Chemical Engineering Science, 2008, 63(12): 3088-3099.

De Yoreo, J. J., Gilbert, P. U. P. A., Sommerdijk, N. A. J. M., et al. Crystallization by particle attachment in synthetic, biogenic, and geologic environments. Science, 2015, 349(6247): aaa6760.

Dutka, F., Starchenko, V., Osselin, F., et al. Time-dependent shapes of a dissolving mineral grain: Comparisons of simulations with microfluidic experiments. Chemical Geology, 2020, 540: 119459.

Fazeli, H., Masoudi, M., Patel, R. A., et al. Pore-scale modeling of nucleation and growth in porous media. ACS Earth and Space Chemistry, 2020, 4(2): 249-260.

Fernandez-Martinez, A., Hu, Y., Lee, B., et al. In situ determination of interfacial energies between heterogeneously nucleated $CaCO_3$ and quartz substrates: Thermodynamics of $CO_2$ mineral trapping. Environmental Science & Technology, 2013, 47(1): 102-109.

Gärttner, S., Frolkovič, P., Knabner, P., et al. Efficiency and accuracy of micro-macro models for mineral dissolution. Water Resources Research, 2020, 56(8): e2020WR027585.

Hommel, J., Coltman, E., Class, H. Porosity-permeability relations for evolving pore space: A review with a focus on (bio-)geochemically altered porous media. Transport in Porous Media, 2018, 124(2): 589-629.

Langer, J. S. Instabilities and pattern formation in crystal growth. Reviews of Modern Physics, 1980, 52(1): 1-28.

Li, H., Hu, Q., Zhu, R., et al. Reactive transport modeling of water-$CO_2$-rock interactions in clay-coated sandstones and implications for $CO_2$ storage. Advances in Geo-Energy Research, 2025, 17(2): 121-134.

Li, H., Wang, F., Wang, Y., et al. Phase-field modeling of coupled reactive transport and pore structure evolution due to mineral dissolution in porous media. Journal of Hydrology, 2023, 619: 129363.

Li, L., Zhang, D., Su, Y., et al. Microfluidic insights into $CO_2$ sequestration and enhanced oil recovery in laminated shale reservoirs: Post-fracturing interface dynamics and micro-scale mechanisms. Advances in Geo-Energy Research, 2024a, 13(3): 203-217.

Li, Q., Fernandez-Martinez, A., Lee, B., et al. Interfacial energies for heterogeneous nucleation of calcium carbonate on mica and quartz. Environmental Science & Technology, 2014, 48(10): 5745-5753.

Li, Q., Steefel, C. I., Jun, Y. Incorporating nanoscale effects into a continuum-scale reactive transport model for $CO_2$-deteriorated cement. Environmental Science & Technology, 2017, 51(18): 10861-10871.

Li, X., Huang, H., Meakin, P. A three-dimensional level set simulation of coupled reactive transport and precipitation/dissolution. International Journal of Heat and Mass Transfer, 2010, 53(13): 2908-2923.

Li, Y., Xu, T., Xin, X., et al. Multi-scale comprehensive study of the dynamic evolution of permeability during hydrate dissociation in clayey silt hydrate-bearing sediments. Advances in Geo-Energy Research, 2024b, 12(2): 127-140.

Liu, J., Xie, X., Meng, Q., et al. Effects of membrane structure on oil-water separation by smoothed particle hydrodynamics. Membranes, 2022, 12(4): 387.

Loomer, D. B., MacQuarrie, K. T. B., Al, T. A. Reactive transport modeling of natural gas molecular and isotopic evolution during diffusive transport in the subsurface. Water Resources Research, 2021, 57(12): e2021WR030702.

Mullins, W. W., Sekerka, R. F. Stability of a planar interface during solidification of a dilute binary alloy. Journal of Applied Physics, 1964, 35(2): 444-451.

Nilsson, Ö., Sternbeck, J. A mechanistic model for calcite crystal growth using surface speciation. Geochimica Et Cosmochimica Acta, 1999, 63(2): 217-225.

Noiriel, C., Soulaine, C. Pore-scale imaging and modelling of reactive flow in evolving porous media: Tracking the dynamics of the fluid-rock interface. Transport in Porous Media, 2021, 140(1): 181-213.

Plummer, L. N., Busenberg, E. The solubilities of calcite, aragonite and vaterite in $CO_2$-$H_2O$ solutions between 0 and 90 °C, and an evaluation of the aqueous model for the system $CaCO_3$-$CO_2$-$H_2O$. Geochimica Et Cosmochimica Acta, 1982, 46(6): 1011-1040.

Prasianakis, N. I., Curti, E., Kosakowski, G., et al. Deciphering pore-level precipitation mechanisms. Scientific Reports, 2017, 7(1): 13765.

Ray, N., van Noorden, T., Frank, F., et al. Multiscale modeling of colloid and fluid dynamics in porous media including an evolving microstructure. Transport in Porous Media, 2012, 95(3): 669-696.

Soulaine, C., Roman, S., Kovscek, A., et al. Mineral dissolution and wormholing from a pore-scale perspective. Journal of Fluid Mechanics, 2017, 827: 457-483.

Starchenko, V. Pore-scale modeling of mineral growth and nucleation in reactive flow. Frontiers in Water, 2022, 3: 800944.

Starchenko, V., Marra, C. J., Ladd, A. J. C. Three-dimensional simulations of fracture dissolution. Journal of Geophysical Research: Solid Earth, 2016, 121(9): 6421-6444.

Steefel, C. I., Molins, S., Trebotich, D. Pore scale processes associated with subsurface $CO_2$ injection and sequestration. Reviews in Mineralogy and Geochemistry, 2013, 77(1): 259-303.

Szymczak, P., Ladd, A. J. C. Reactive-infiltration instabilities in rocks. Fracture dissolution. Journal of Fluid Mechanics, 2012, 702: 239-264.

Tian, H., Xu, T., Zhu, H., et al. Heterogeneity in mineral composition and its impact on the sealing capacity of caprock for a $CO_2$ geological storage site. Computers & Geosciences, 2019, 125: 30-42.

Tian, Z., Wang, J. Lattice boltzmann simulation of dissolution-induced changes in permeability and porosity in 3d $CO_2$ reactive transport. Journal of Hydrology, 2018, 557: 276-290.

Wang, H., Cai, J., Su, Y., et al. Pore-scale study on shale oil-$CO_2$-water miscibility, competitive adsorption, and multiphase flow behaviors. Langmuir, 2023, 39(34): 12226-12234.

Yang, B., Xu, T., Du, Y., et al. Numerical investigation on the influence of $CO_2$-induced mineral dissolution on hydrogeological and mechanical properties of sandstone using coupled lattice boltzmann and finite element model. Journal of Hydrology, 2024a, 639: 131616.

Yang, F., Guan, D., Starchenko, V., et al. Effect of nucleation heterogeneity on mineral precipitation in confined environments. Geophysical Research Letters, 2024b, 51(9): e2023GL107185.

Yang, F., Stack, A. G., Starchenko, V. Micro-continuum approach for mineral precipitation. Scientific Reports, 2021, 11(1): 3495.